Shock-induced microstructural response of mono- and nanocrystalline SiC ceramics

Paulo S. Branicio, Jingyun Zhang, José P. Rino, Aiichiro Nakano, Rajiv K. Kalia, and Priya Vashishta
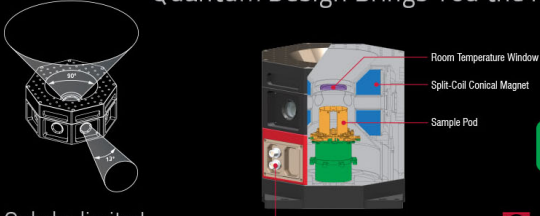
Shock-induced microstructural response of mono- and nanocrystalline SiC ceramics

Paulo S. Branicio,[1,2,a)] Jingyun Zhang,[3,4] José P. Rino,[5] Aiichiro Nakano,[2] Rajiv K. Kalia,[2] and Priya Vashishta[2]

[1]*Mork Family Department of Chemical Engineering and Materials Science, University of Southern California, Los Angeles, California 90089, USA*
[2]*Collaboratory for Advanced Computing and Simulations, Departments of Chemical Engineering and Materials Science, Physics and Astronomy, Computer Science, and Biological Sciences, University of Southern California, Los Angeles, California 90089, USA*
[3]*Jiangsu Key Laboratory for Optoelectronic Detection of Atmosphere and Ocean, Nanjing University of Information Science and Technology, Nanjing 210044, China*
[4]*School of Physics and Optoelectronic Engineering, Nanjing University of Information Science and Technology, Nanjing 210044, China*
[5]*Department of Physics, Universidade Federal de São Carlos, Rodovia Washington Luís, km 235, São Carlos, SP, Brazil*

The dynamic behavior of mono- and nanocrystalline SiC ceramics under plane shock loading is revealed using molecular-dynamics simulations. The generation of shock-induced elastic compression, plastic deformation, and structural phase transformation is characterized at different crystallographic directions as well as on a 5-nm grain size nanostructure at 10 K and 300 K. Shock profiles are calculated in a wide range of particle velocities 0.1–6.0 km/s. The predicted Hugoniot agree well with experimental data. Results indicate the generation of elastic waves for particle velocities below 0.8–1.9 km/s, depending on the crystallographic direction. In the intermediate range of particle velocities between 2 and 5 km/s, the shock wave splits into an elastic precursor and a zinc blende-to-rock salt structural transformation wave, which is triggered by shock pressure over the ∼90 GPa threshold value. A plastic wave, with a strong deformation twinning component, is generated ahead of the transformation wave for shocks in the velocity range between 1.5 and 3 km/s. For particle velocities greater than 5–6 km/s, a single overdriven transformation wave is generated. Surprisingly, shocks on the nanocrystalline sample reveal the absence of wave splitting, and elastic, plastic, and transformation wave components are seamlessly connected as the shock strength is continuously increased. The calculated strengths 15.2, 31.4, and 30.9 GPa for ⟨001⟩, ⟨111⟩, and ⟨110⟩ directions and 12.3 GPa for the nanocrystalline sample at the Hugoniot elastic limit are in excellent agreement with experimental data. *Published by AIP Publishing.*
https://doi.org/10.1063/1.5023915

I. INTRODUCTION

SiC is a well-known high strength ceramic material with outstanding properties that have been used in a wide range of applications, in particular, those involving extreme conditions of pressure, temperature, and wear such as in nuclear reactor cladding,[1–3] abrasives,[4] and gas turbines.[5] Owing to the low density and high strength, SiC is also an ideal material for armor.[6,7] For the latter application, it is essential to understand the behavior of SiC under extreme conditions. Those are typically found in studies of strong shock loading. The literature of such studies with high strength ceramics similar to SiC is extensive and includes shock experiments and continuum modeling on materials such as Al_2O_3, B_4C, Si_3N_4, and AlN.[6,8–10]

Several experimental investigations have been performed to investigate the shock response of SiC. The strength of SiC was compared to that of B_4C in shock experiments revealing that while the latter showed a higher Hugoniot elastic limit

(HEL), ∼20 GPa, than the former, ∼16 GPa, SiC showed an increasing strength with additional deformation, in striking contrast with B_4C, which showed a severe loss in strength.[11] An intriguing delayed failure was reported in different grades of SiC based on plate impact and split Hopkinson pressure bar experiments.[12] Follow-up experiments indicated that this behavior was related to an interplay between plastic (PL) deformation and brittle failure.[13] The shock Hugoniot has been evaluated at different SiC structures at pressures up to 160 GPa (Refs. 14–16) setting the observed phase transition pressure threshold at ∼105 GPa. The pressure induced transformation in SiC was independently confirmed at ∼104 GPa, with a volume change of 9%, in experiments of plane impact used to evaluate the strength of SiC in Hugoniot states.[16] The evolution of shock waves was investigated in different SiC samples using independent techniques,[17,18] which indicate high longitudinal sound waves of ∼11.5 km/s, high HEL in excess of ∼9 GPa, and high dynamic tensile strength (spall strength) of more than 0.5 GPa. A combination of experiments and atomistic modeling of impact on SiC was employed to describe the general trends of the generation and propagation

a)Author to whom correspondence should be addressed: branicio@usc.edu

of shock waves and the shock induced fracture dynamics.[19] So far, to the best of our knowledge, there is scarce atomistic modeling performed on SiC under shock to complement the vast experimental data available and further advance the understanding of the complex behavior of SiC under extreme conditions.

Atomistic insights could clarify the shock induced structural transformation in SiC at different shock intensities. The elusive presence and the role of shock induced plastic deformation could also be further understood from atomistic modeling as well as the effect of crystallographic directions and interfaces. Molecular dynamics (MD) modeling of plane shock loading has been widely used to investigate materials under extreme conditions and is an ideal tool for that purpose. MD simulations of shock have been performed for over several decades to provide insightful details on shock propagation and describe shear stress relaxation mechanisms that may involve complex structural transitions and chemical reactions.[20–24] Large scale MD simulations of shock, allowing the modeling of much larger multi-million atom systems, present a new dimension for the understanding of shock, narrowing the gap between experimental studies and microscopic accounts of shock phenomena.[25–28]

Nonetheless, realistic MD simulations of shock in ceramics are scarce. AlN and Al_2O_3 have been the subject of recent large scale MD simulations of projectile impact.[29–32] These works offered a detailed view of the damage generated by projectile impact in these ceramics, which includes shock induced plasticity and brittle fracture as a result of shock release. Plane shock loading on the other hand offers an ideal platform to investigate the intrinsic effects of shock loading on ceramics. The detailed structure of the shock waves can be investigated closely following its propagation across the material. Branicio *et al.*[29] have performed simulations of plane shock to investigate the complex behavior of crystalline AlN ceramics to strong shock loading. As mentioned

previously, a preliminary 2D atomistic modeling of impact on SiC has been reported and provided useful insights into the shock effects in ceramics.[19] However, realistic 3D models are required to reveal the complex deformation mechanisms in SiC that includes plastic deformation and structural phase transformation (SPT) induced by high pressure. The related topic of shock spall on SiC was recently discussed by Li *et al.*[33] It was reported that SiC displays different spall regimes from classical spall to micro-spall as particle velocity is increased beyond 0.5 km/s. Recently, a more realistic atomistic modeling of shock on SiC was performed using a Tersoff potential.[34] They demonstrated in detailed 3D simulations the formation of split shock waves and the generation of well-defined elastic, plastic, and transformation waves under increasingly intensive shocks. However, many questions remain unanswered due to deficiencies of the Tersoff potential, e.g., it does not have any silicon to carbon charge transfer terms included in it. Therefore, a realistic description of experimental shock features is still lacking. For instance, it is not clear what the effects of crystallographic directions, temperature, and interfaces on the SiC shock profile are.

Here, large scale MD simulations are employed to investigate the response of 3C-SiC (SiC in the zinc blend cubic phase) ceramics under planar shock waves considering explicitly the effects of low-index crystallographic directions as well as temperature, and grain boundary interfaces. Figure 1 shows illustrations of the different models used in our work. The forces among Si and C atoms are derived from an effective many-body interatomic potential validated by experimental elastic constants, melting temperature, vibrational density of states, and specific heat.[35] A more stringent validation of the potential is provided by the zinc blende-to-rock salt structural phase transition. High-pressure experiments reveal that this transformation occurs at ∼100 GPa which is the value predicted in good agreement in the simulations.[35,36] This potential has been used successfully to describe SiC fracture dynamics[37] and high
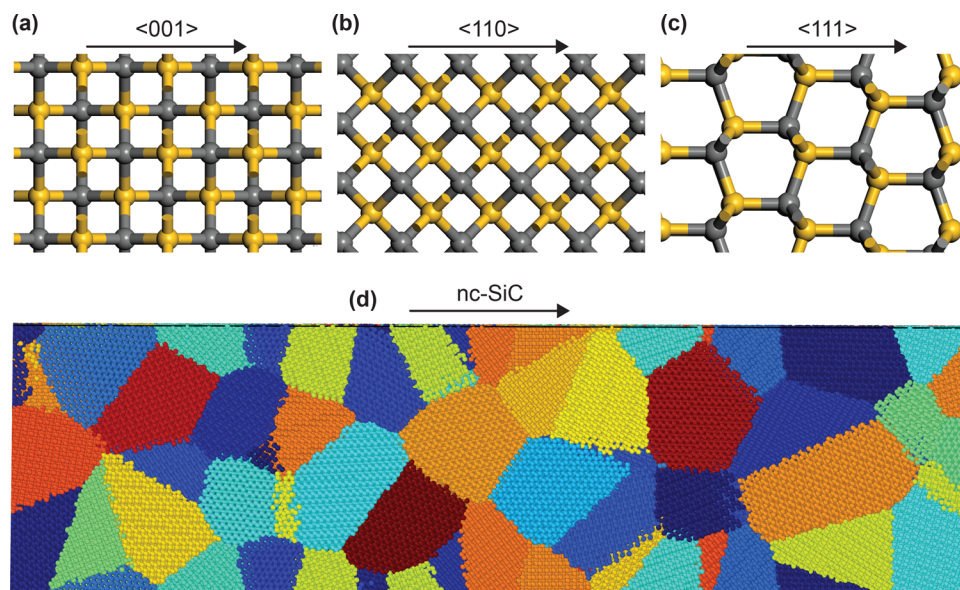

FIG. 1. Illustrations of the SiC models simulated. Simulations are performed on monocrystalline models with the impact direction aligned with (a) $\langle 001 \rangle$, (b) $\langle 110 \rangle$, and (c) $\langle 111 \rangle$ directions, as well as with a (d) nanocrystalline model with 5 nm average grain size. In (a)–(c), silicon and carbon atoms are colored yellow and gray, while in (d) neighbor grains are colored differently to highlight the nanostructure. The arrows indicate the direction of the shock propagation.

strain-rate deformation of nanowires.[38] The same potential form has also been successfully applied to describe the mechanical behavior of similar ceramics such as AlN[29,39,40] and Al$_2$O$_3$.[32,41] The ability of the potential to accurately describe the response of SiC to extreme conditions was previously demonstrated by investigating the shock induced ductility in projectile impacts.[30] Very recently, a comparison of different interatomic potential for SiC under shock was performed showing the superiority of the Vashishta potential.[42]

II. SIMULATION DETAILS

Slabs with dimensions about $12 \times 12 \times 200$ nm^3, containing roughly three million atoms, are simulated. Both monocrystalline 3C-SiC and nanocrystalline samples with grains of 3C-SiC structure are considered. For monocrystalline samples, plane shock loading is performed along the $\langle 001 \rangle$, $\langle 110 \rangle$, and $\langle 111 \rangle$ low-index crystallographic directions; please see Figs. 1(a) to 4(c). The long system slab dimension, chosen as the z direction, is aligned with the impact direction to allow shock waves to propagate across the system and develop for up to 18 ps. The nanocrystalline SiC (nc-SiC) sample is generated using the Voronoi tessellation method.[43] We used an average grain size $d = 5$ nm, an illustration of the initial relaxed nanostructure is shown in Fig. 1(d). The centers chosen for the tessellations are randomly distributed points within the sample. Points closer than 0.4 d are removed to avoid the generation of unphysical grains with very large aspect ratios. Once the grain microstructure is obtained, the atomic positions are chosen by randomly assigning a crystallographic orientation to each grain and then placing atoms on sites of the appropriately oriented 3C-SiC lattice. The nc-SiC nanocrystals are annealed to minimize low or high-density regions near the grain boundaries (GB) and triple junctions. Annealing is also used to relax the GB interfaces and minimize the residual stresses. A similar procedure was used in an earlier investigation of grain size effects of SiC in its mechanical properties.[44] Simulations are performed with periodic boundary conditions in the lateral x and y directions and free surfaces in the impact z direction. The planar shock wave is generated using a reverse geometry with the system hitting a stationary "piston," implemented as a momentum mirror. Such hard wall piston elastically bounces any particle hitting its surface. The particle velocity U$_p$, which is the impact velocity, is chosen to be in the wide range from 0.1 to 6.0 km/s to access all shock regimes and induce shock stresses as high as 280 GPa. The corresponding strain rates are in the range of 5×10^8 s^{-1} to 3×10^{10} s^{-1}. The atomic equations of motion are integrated with a time step of 1 fs. Analyses of physical properties are carried out along the impact direction using bins 7.5 Å wide. The calculated shock profiles include properties such as particle velocity, stress, internal energy, displacement in the xy plane, and density. In particular, an accurate local density is calculated based on the inverse atomic Voronoi polyhedral volume. Such volumes calculated from the Voronoi Tessellation[43] defined by the local crystalline topology give the space occupied by the atoms in the crystal and its inverse, when averaged locally, gives an accurate measure of the local density, which is essential in the calculation of the local stresses.[45] All MD simulations are performed with our own parallel simulation code which have been used previously in many different studies of SiC and related ceramics.[29,30,37,39–41,46–48]

III. RESULTS AND DISCUSSION

The shock Hugoniot curve describing the relationship between shock wave velocities as a function of particle velocity is one of the most important information one may get to describe the shock response of a material. The shock Hugoniot from simulations performed on SiC at T = 10 K and T = 300 K for different low-index crystallographic directions of the 3C-SiC structure as well as nanocrystalline SiC (nc-SiC) is plotted at Fig. 2. We have found three major regimes for the shock response, which agree very well with the experiments. The calculated shock velocities as a function of particle velocities are compared with three independent experimental results.[14–16] The experiments are done on diverse microcrystalline samples. In reported experiments,[15,16] the average grain size was 4 μm and samples had predominantly the 6H polytype. In Fig. 2, open symbols indicate experimental data in contrast with the MD data displayed with solid symbols. 3C-SiC monocrystals are expected to have an anisotropic response to shock loading. Therefore, simulations are performed considering the three low-index crystallographic directions of 3C-SiC, i.e., with the $\langle 001 \rangle$, $\langle 110 \rangle$, and $\langle 111 \rangle$ directions aligned along the shock direction. Since the response of the 5-nm grain size nc-SiC model is expected to be isotropic, as the polycrystalline experimental samples, only one simulation is performed for it.

For particle velocities below a given threshold, that depends exactly on the model and temperature, the simulations show the presence of elastic shock waves propagating with constant velocity. However, the simulation data indicate that the single solitary longitudinal elastic shock is split into two elastic waves before any plastic deformation is generated that occurs for directions $\langle 001 \rangle$ and $\langle 111 \rangle$. In Fig. 2, the pairs of elastic waves are named EL1 and EL2, while the plastic and structural transformation waves are referred to as PL and SPT. For the crystalline samples, well-defined wave configurations can be identified: For particle velocity between $\sim 0.8–1.9 < $ U$_p$ $\lesssim 2.5–3$ km/s, four coordinated intermediate phase (EL2) and plastic (PL) waves coexist with a faster elastic wave (EL1). From $\sim 2.25–3 < $ U$_p$ < 5 km/s, a structural phase transformation (SPT) coexists with the longitudinal faster elastic wave (EL1). From 5–6 km/s, a single overdriven wave is present. Results at both temperatures indicate essentially the same regimes. Therefore, in the remaining discussion, the data obtained at 10 K will be mostly used since the temperature fluctuations in those data are minimum, facilitating the analysis. The regimes of shock generated for SiC for the different crystallographic directions as well as for the nc-SiC sample are in excellent agreement given the differences in sample structures. Below, each of the different shock regimes identified is discussed in detail.

Purely elastic waves are generated for weak shocks in SiC with U$_p$ < 0.8 km/s. Increasing the shock strength, one reaches the end of the regime of purely elastic shock generation that indicates the Hugoniot elastic limit. The data in Fig. 2 indicate that the threshold particle velocity for this regime in
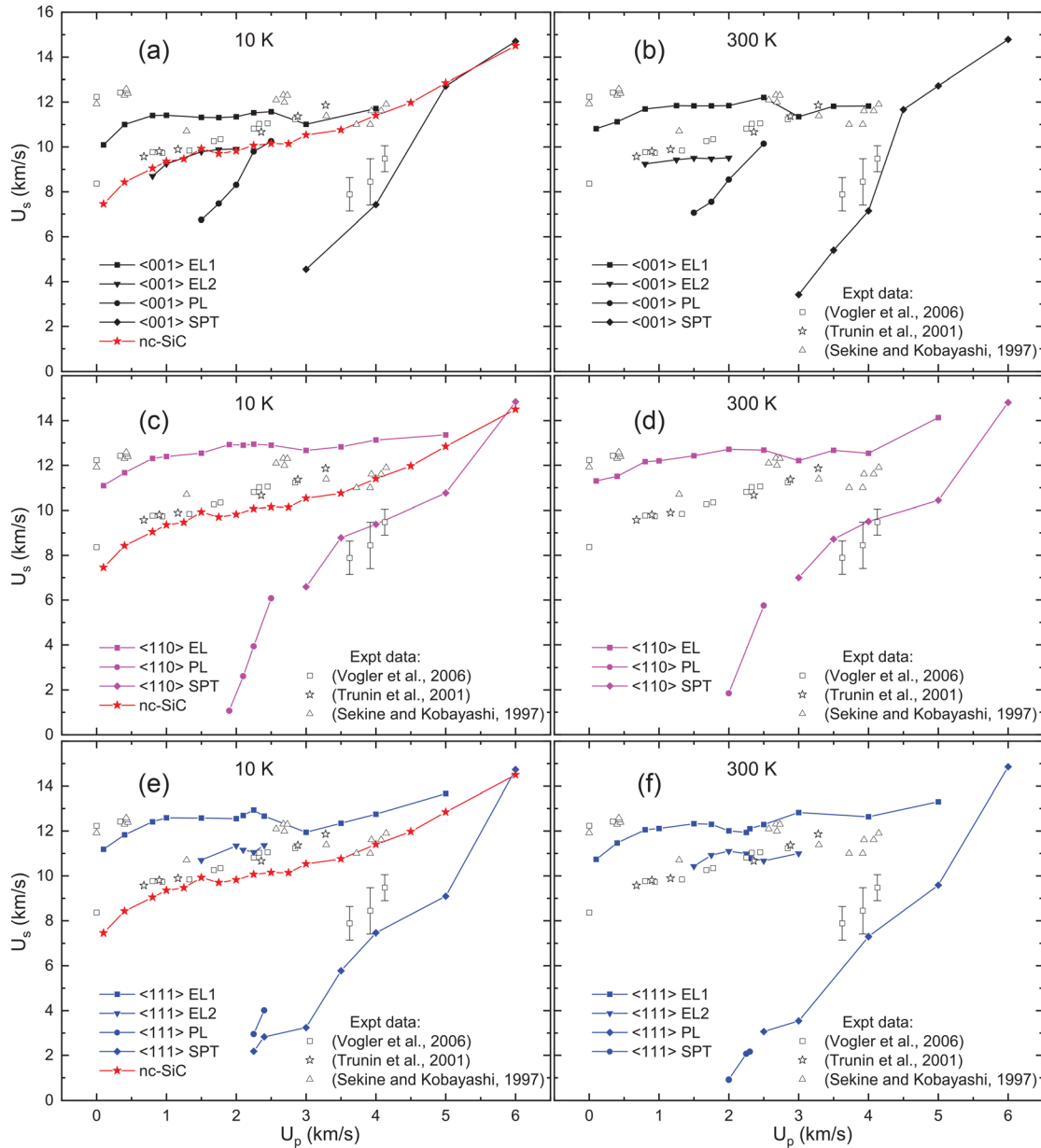
FIG. 2. SiC shock Hugoniot for the low index crystallographic directions of the 3C-SiC structure as well as nanocrystalline SiC. (a), (c), and (e) data for T = 10 K and (b), (d), and (f) data for T = 300 K. Filled (open) symbols indicate MD (experimental) data. EL1, EL2, PL, and SPT indicate elastic waves 1 and 2, plastic wave, and structural phase transformation wave. MD results for monocrystals have the ⟨001⟩ (a) and (b), ⟨110⟩ (c) and (d), and ⟨111⟩ (e) and (f) directions aligned with the shock direction. Both the simulated 5 nm grain size nanocrystalline model and the polycrystalline experimental samples are isotropic and their curves are shown in all plots for comparison. For the crystalline samples, well-defined wave configurations can be identified: For particle velocity between ∼1–1.5 < U_p ≲ 2.5–3 km/s, four coordinated intermediate phase (EL2) and plastic (PL) waves coexist with a faster elastic wave (EL1); from ∼2.25–3 < U_p < 5 km/s, a structural phase transformation (SPT) wave coexists with a faster elastic wave (EL1), and at 6 km/s and beyond, a single overdriven wave is present. EL2 is not present for ⟨110⟩ direction. The Hugoniot curve for the nc-SiC model indicates no wave splitting in the whole range of particle velocities considered. Results at both temperatures indicate essentially the same response regimes.

monocrystalline samples is in the range $U_p = 0.8$–1.9 km/s that is in good agreement with the polycrystalline experimental data which show the beginning of a region of plastic phase just beyond $U_p \sim 0.5$ km/s. The elastic shock waves are quantified along different crystallographic directions by calculating profiles of several physical quantities in the system along the shock propagation. Figure 3(a) shows an atomic structure region in the system highlighting the shock front region and the elastically compressed regions in the two elastic waves generated along the direction ⟨111⟩ at $U_p = 1.5$ km/s. Figures 3(b) to 3(e) show shock profiles with particle velocity, density,

and stress showing the well-defined elastic wave split. Abrupt changes in particle velocity along the system are the most important signature of the presence and split of shock waves. Figure 3(b) shows that particle velocity suddenly changes to ∼1.1 km/s at the elastic wave front and maintains that value until the arrival of the second elastic wave when it reaches quickly the impact particle velocity 1.5 km/s. Other quantities, such as density, stress, energy, and temperature also change abruptly in the shock wave front. Figure 3(c) quantifies the elastic compression of the system by the two elastic waves. At the elastic fronts, the density increases from 3.21 g/cm^3 to
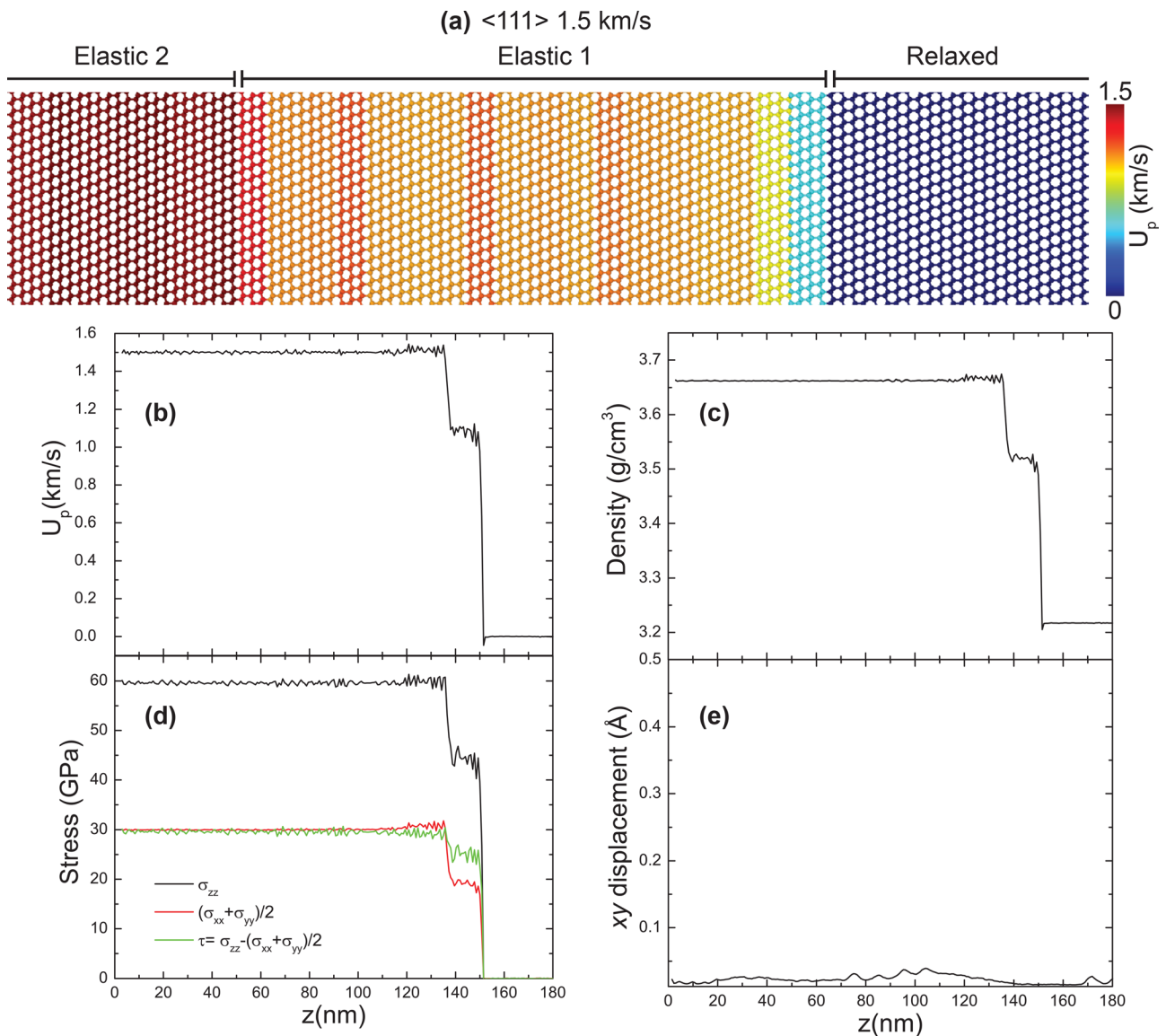
FIG. 3. Atomic structure and shock profiles of elastic waves along the ⟨111⟩ direction for $U_p = 1.5$ km/s. (a) Atomic structure with atoms colored by the particle velocity indicating a clear elastic wave split. (b)–(d) Particle velocity, density, and stress profiles showing a sharply defined elastic wave split. (e) xy displacement profile indicating residual perpendicular atomic displacement typical of elastic waves. Besides the longitudinal elastic wave (Elastic 1), an additional elastic wave (Elastic 2) traveling slightly slower than the first also propagates along the ⟨111⟩ direction and corresponds to a tetragonal intermediate phase which is also generated for elastic compression along the <001> direction.

3.52 g/cm³ (EL1) and then to 3.66 g/cm³ (EL2). The stress profile in Fig. 3(d) shows that the shear stress is accumulated progressively in the system with the arrival of the two elastic waves. A useful quantity to distinguish elastic waves from plastic and transformation waves is the average displacement perpendicular to the impact direction. Figure 3(e) shows the average displacement of the particles in the xy plane, transverse to the shock direction, which indicates accurately the threshold for plasticity. As can be seen in Fig. 3(e), only residual displacement generated by the thermal fluctuations in their position is present.

The second elastic wave generated for moderate shocks corresponds to an intermediate structure generated prior to the structural phase transformation and plastic waves. Prompted by the shock results, we perform additional simulations with a fully periodic bulk 3C-SiC system to further understand this phase. The system is simulated at quasi-static conditions at a hydrodynamic pressure ramp from 0 to 101 GPa. Radial distribution functions and bond angle analysis are calculated to quantify the change in the atomic structure as a function of pressure. The results illustrating the significant change in correlation functions are shown in Fig. 4. The radial distribution function and coordination number displayed in Fig. 4(a) clearly show a change in the structure from 64 GPa to 90 GPa. However, as can be seen from the coordination number, the structure is still 4-coordinated. From 90 GPa to 101 GPa, the g(r) function shows a drastic change to a 6-coordination structure. The bond angle analysis shown in Fig. 4(b) indicates that this six-coordinated structure has equilibrium Si-C-Si bonds at ∼90° and 180°, which shows a typical function of a rock salt structure. At 65 GPa, the bond angle distribution shows the typical peak at 109° of the zinc blende structure. However, at both 75 GPa and 90 GPa, the bond angle distribution shows an intermediate structure with peaks at ∼98° and
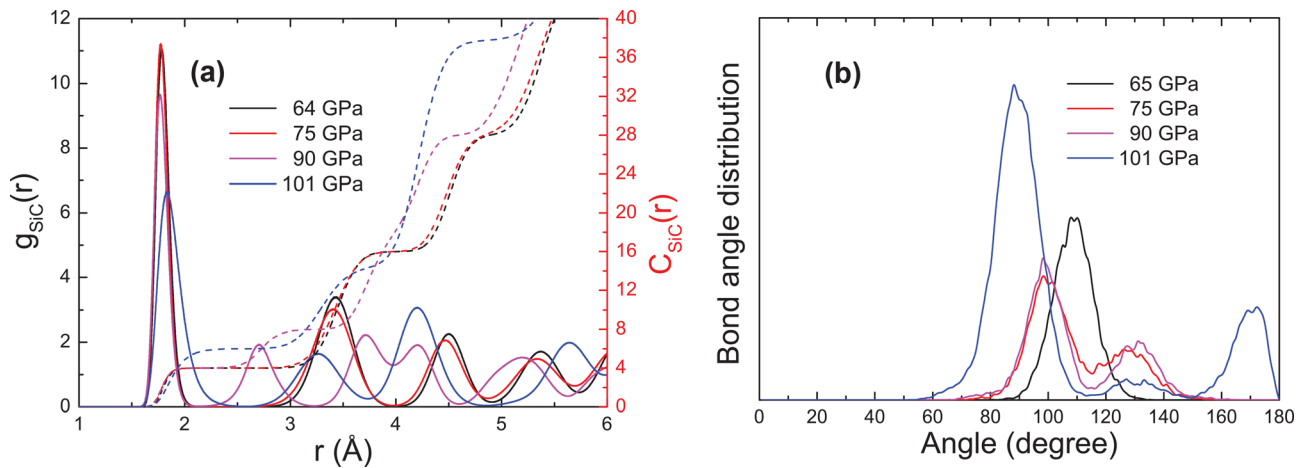
FIG. 4. Correlation functions for 3C-SiC as a function of hydrostatic pressure. (a) Radial distribution functions and coordination numbers for Si-C pairs as a function of pressure in solid and dashed lines, respectively. (b) Bond angle distribution in arbitrary units as a function of pressure. Curves at 64/65 GPa indicate the typical four coordinated zinc blend structure. Curves at 75 and 90 GPa indicate a tetragonal intermediate phase which is clearly reproduced under dynamic conditions of the shock simulations. Curves at 101 GPa indicates a typical six coordinated rock salt structure.

$127°$ (75 GPa) and $130°$ (90 GPa). These combined results indicate that at 75 GPa and 90 GPa, 3C-SiC undergoes a deformation, which is compatible with an elastic deformation of the structure into a tetragonal structure. Such an intermediate structure was not discussed previously for SiC.[35] However, as can be seen in Fig. 7 of that publication, the bond distance curve as a function of pressure indicates the presence of an intermediate structure between the zinc blende and the rock salt. Intermediate phases in the pressure induced structural phase transformation of SiC studied by first principles have in fact been proposed previously and include tetragonal and orthorhombic states.[51] For more details on this intermediate tetragonal phase, the reader is referred to this first principles investigation.

As shown in Fig. 2, the regime of elastic compression gives rise to irreversible deformation on increasing shock intensity. For particle velocity above 1.5–3 km/s, depending on the crystallographic direction, a plastic wave is generated. Its signs are clear for impact on all crystallographic directions. In Fig. 5, the atomic structure and shock profiles are shown for a typical plastic regime observed in the simulations. Figure 5 shows the data for the direction $\langle 110 \rangle$ for impact at $U_p = 2.5$ km/s. Plastic waves can take different forms and commonly involve dislocation plasticity, which is particularly the case for shocks on metallic materials.[28,49,50] However, ceramics such as SiC have an outstanding resistance to plastic deformation, in particular to dislocation plasticity. Monocrystal simulations of plane shock loading on AlN have shown very restricted plastic deformation prior to structural phase transformation into high pressure phases.[39] A similar high resistance to dislocation plasticity is expected from SiC. However, SiC in its cubic phase (3C-SiC) have many available easy planes for dislocation glide. Previous simulations of projectile impact on 3C-SiC have demonstrated that in fact under suitable conditions a dense network of dislocation lines can be generated.[30] The results for shock on different crystallographic directions indicate that under plane shock conditions 3C-SiC plastic deformation wave have predominately deformation twinning as its primary deformation mode. The atomic structure at Fig. 5(a) shows a typical

profile of the onset deformation twinning process present in the plastic waves generating initially a dense pack of twins along the $\langle 110 \rangle$ direction. The initially highly packed twins with thickness of $\sim$2–4 nm gradually coarse and their thickness grow up to $\sim$12 nm during the short simulation time. The atomic displacement from initial positions is highlighted by the atomic x displacement, with x being the vertical direction on the figure. The particle velocity profile shown in Fig. 5(b) indicates a sharp increase in particle velocity at the elastic shock front to about 1.8 km/s which is followed by a gradual increase to the impact particle velocity of 2.5 km/s at the diffuse plastic wave front. The density profile shown in Fig. 5(c) indicates more clearly the plastic wave front located at $\sim$106 nm. At that point, the elastically compressed material at 3.72 g/cm^3 is gradually compressed to $\sim$4.3 g/cm^3 by the plastic wave. The plastic wave front is also clearly defined by the stress profile shown in Fig. 5(d). The initial strong shear stress generated by the longitudinal elastic compression of $\sim$36 GPa is gradually released as the plastic deformation wave develops. The final shear stress calculated close to the impact surface is close to 10 GPa. A clear sign of plastic deformation is the sharp increase in atomic displacement on the plane perpendicular to the impact direction. Figure 5(e) indicates that at the plastic shock front the average xy displacement increases sharply and continues to do so as the deformation twinning takes place in the system. Large average atomic displacements of over 6 Å are observed in the plastically deformed region.

The shock Hugoniot displayed in Fig. 2 indicates that at $U_p = 3$ km/s a SPT wave is generated and drives the system from the low-pressure zinc blende phase to the high pressure compact rock salt phase. The results for different crystallographic directions agree well with the experimental data,[16] also displayed in Fig. 2, which indicates a transformation wave starting at $\sim$3.6 km/s. To illustrate the SPT wave, the atomic structure and shock profiles from the simulation with $U_p = 4.0$ km/s along the $\langle 111 \rangle$ direction are shown in Fig. 6. As can be seen in Fig. 6(a), the atomic structure undergoes a sharp structural transformation from the 4-coordinated zinc blende phase, shown by blue atoms, to 6 coordinated phase
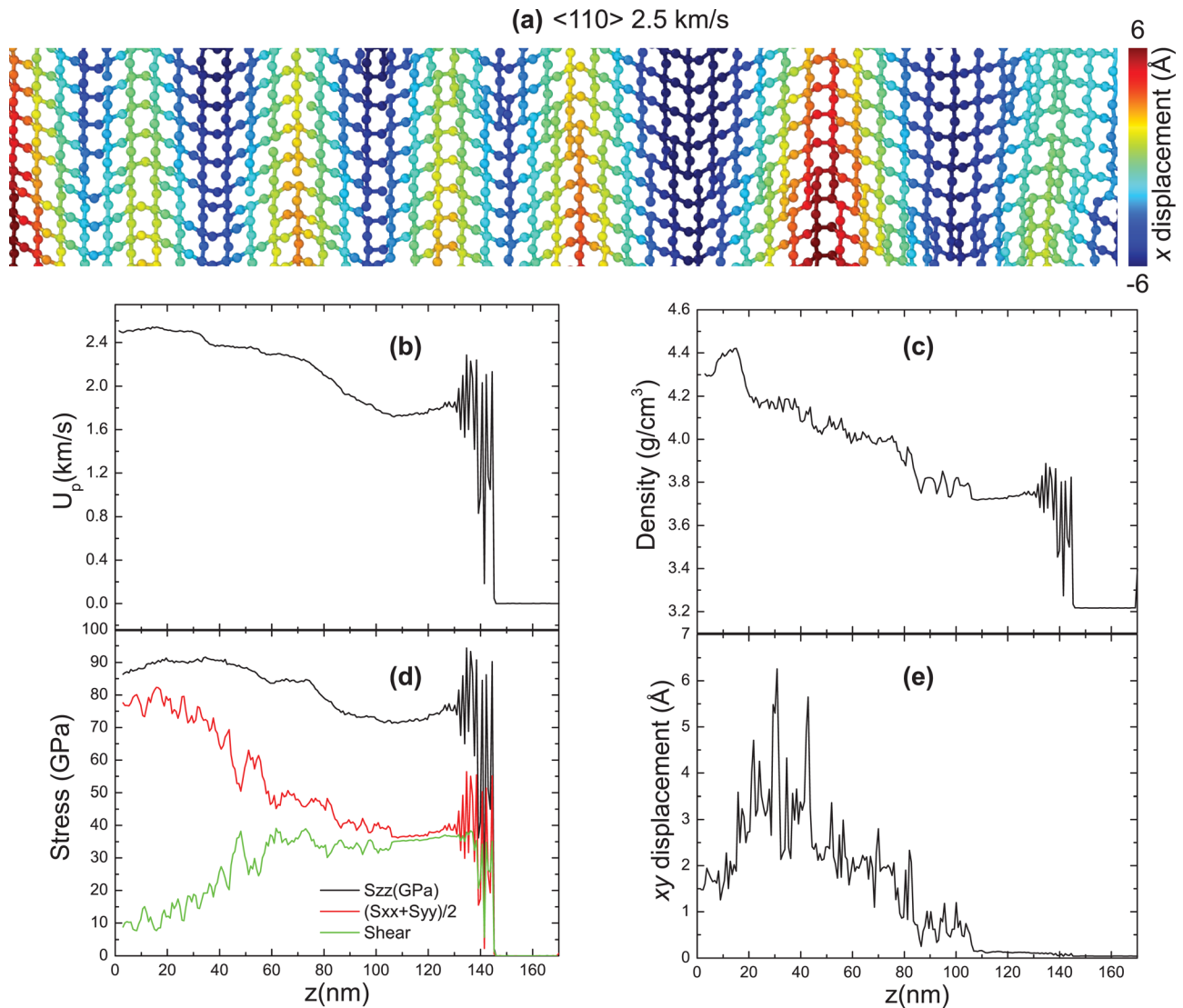
FIG. 5. Atomic structure and shock profiles of plastic deformation along $\langle 110 \rangle$ direction for $U_p = 2.5$ km/s. (a) Layer of atoms along the impact direction highlighting the deformation twinning character of the plastic wave. Colors indicate the displacement along the perpendicular direction to the shock, on the page plane. (b) Particle velocity profile indicating the gradual increase in particle velocity till the maximum value in the plastic region. (c) Density profile showing uncompressed material and the material compressed by the plastic wave to the range from 3.9 to 4.4 g/cm³. (d) Stress profile indicates that the plastic wave effectively releases most of the built-up shear stress of the shock front. (e) The *xy* displacement profile along the system indicates that deformation twinning generates a large atomic displacement of up to 6 Å.

rock salt, shown in red. The color of the atoms is based on the value of the centrosymmetry parameter which also indicates a heterogeneous transformation in the shocked material with a high density of atoms at intermediate structures spread across the whole sample. These atoms represent defects, grain boundaries, or atoms undergoing the transformation at intermediate structures. While the transformation is very heterogeneous, the shock profiles shown in Figs. 6(b) to 6(d) indicate that the shock front is relatively sharp and the transformation generates a well-defined transformed state. In particular, the density profile along the shock system displayed in Fig. 6(c) indicates that the elastic precursor compresses the material from 3.21 g/cm³ to 4.21 g/cm³. The transformation shock wave additionally densifies the material to 4.91 g/cm³, which amounts to a 24% volume reduction at the strong elastic compression and an additional 14% volume reduction at the structural transformation. The total

volume reduction at the strong shock at 4.0 km/s generated by the solid-solid transformation therefore amounts to 35%. The structural phase transformation process releases most of the generated shear stress from the elastic wave. As shown in Fig. 6(d), the ∼30 GPa shear stress is quickly released by the transformation and brings the stress state in the transformed material to a nearly hydrostatic state. The *xy* displacement shown in Fig. 6(e) indicates that the transformation process displaces sharply atoms at the shock front by up to 10 Å. However, given the heterogeneous nature of the SPT wave, the value of the displacement varies widely along the transformed material.

Intriguingly, the shock Hugoniot for the nanocrystalline sample does not indicate any sharp split of the shock waves, alike that displayed for the monocrystalline models. Nonetheless, one can still distinguish three regimes separated by the threshold particles velocities at 1.5 km/s and 4.0 km/s.
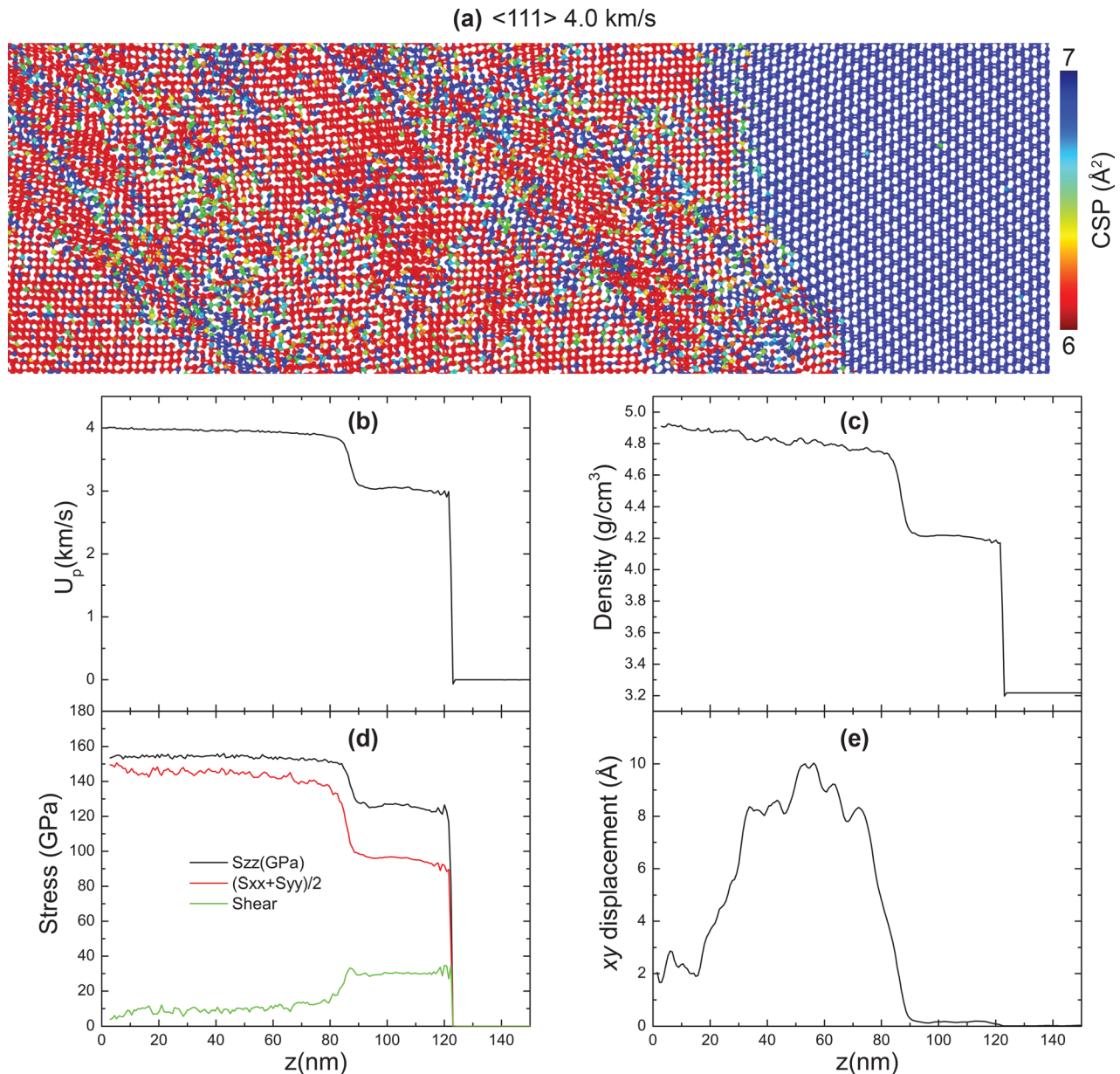
(a) <111> 4.0 km/s

FIG. 6. Atomic structures and shock profiles of the structural phase transformation wave generated for shock along the $\langle 111 \rangle$ direction for $U_p = 4.0$ km/s. (a) Layer of atoms along the impact direction indicates the structural phase deformation wave that drives SiC from the low-pressure zinc blend (blue) to the high-pressure rock salt phase (red). Colors indicate Centrosymmetry parameter (CSP) values. (b) Particle velocity profile indicating the split wave profile with elastic and transformation waves. (c) Density profile showing uncompressed, elastically compressed, and transformed regions. (d) Stress profile indicates the shear stress release of the structural transformation wave. (e) The xy displacement profile along the system indicates that the transformation takes place by locally displacing atoms by up to 10 Å from initial positions on the plane perpendicular to impact direction.

As shown in Fig. 7, below 1.5 km/s, the shear stress accumulates in the nanocrystalline sample, which is indicative of the lack of release mechanisms and the presence of purely elastic compression of the sample. On the other hand, from 1.5 km/s to 3.5 km/s, the shear stress is continuously released indicating the activation of plastic deformations in the material, consistent with the behavior observed for the monocrystalline samples. At 4 km/s, Fig. 7 indicates a sudden increase in shear stress which is then gradually released on increasing particle velocity indicating a shift in release mechanisms, which is consistent with the above described SPT for the monocrystalline models.

A challenging question that remains to be explained is why there is no splitting in the shock Hugoniot observed for

the nanocrystalline models and even more challenging is why the Hugoniot curve follows almost perfectly the experimental curve corresponding to the plastic wave, please see Figs. 2(a), 2(c), and 2(d). One can answer this question by noting the inherently nanocrystalline structure of the sample under discussion. The grains in the nanocrystalline sample are substantially smaller than those in microcrystalline experimental samples. The fraction of softer amorphous interfaces is much larger as well at ~35%. For details on the nanocrystalline sample simulated, the reader is referred elsewhere.[44] When the experimental sample enters the plastic regime, the material increasingly accumulates defects and additional grain boundaries, turning on perspective the structure closer to the nanocrystalline one. On the other hand, the plastic regime
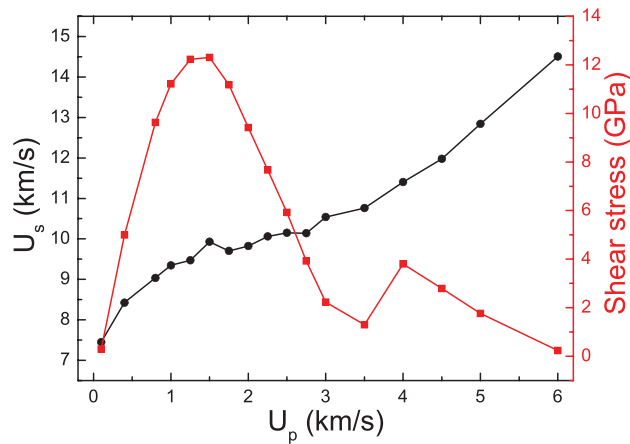
FIG. 7. Shock Hugoniot and shear stress for impact on nc-SiC. Black curve indicates shock velocities while the red curve shows the shear stress as a function of particle velocity. While the shock Hugoniot indicates a nearly monotonic increase in shock speed and absence of wave splitting, the shear stress profile indicates clearly an elastic and two regimes of shear stress release corresponding to a plastic wave and a structural phase transformation wave.
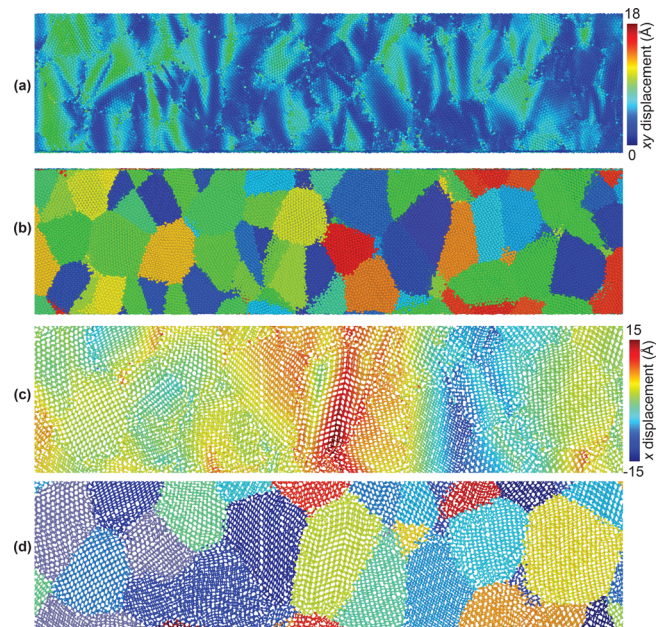

FIG. 8. Atomic structures and local displacement profiles of the plastic deformation in the nc-SiC model for $U_p = 2.5$ km/s. (a) Layer of atoms along the impact direction highlighting that plastic deformation takes place mostly at grain boundary interfaces, e.g., grain boundary sliding. The color gradient indicates displacement in the plane perpendicular to the impact direction (left to right in the page). (b) The nc-SiC nanostructure corresponding to (a) with grains highlighted in different colors. (c) Layer of atoms along the impact direction indicating also the presence of deformation twinning. Atoms are colored according to the displacement perpendicular to the impact direction in the page plane. (d) Nanostructure corresponding to (c).

will not change dramatically the nanocrystalline sample given the already high density of interfaces and structural defects present, which is the main reason why the nanocrystalline sample Hugoniot resembles that of the plastically deformed experimental sample and does not generate wave splits. Entering the structural transformation regime, the same argument is valid and while the shear stress clearly indicates a change in release mechanisms, the Hugoniot indicates a relatively smooth increase in shock velocity.

An aspect to note about the plastic wave in the nanocrystalline sample is that it takes place using deformation mechanisms distinct than those of the monocrystalline models. As shown in Fig. 8, the plastic wave in the nanocrystalline sample takes place using two atomistic mechanisms: grain boundary sliding and deformation twinning. Grain boundary sliding at such small average grain size material is expected to be an important deformation mode. Figure 8(a) shows that in fact the bulk of the plastic deformation present in the plastic wave is generated at or closer to the interfaces as highlighted by the *xy* displacement. For reference, the grains of the nanostructure shown in A are shown in different colors in B. Nonetheless, while the bulk of the deformation occurs at the interfaces, deformation twinning is still active inside grains, as shown in Fig. 8(c). The reference nanostructure for Fig. 8(c) is shown in Fig. 8(d). In contrast with the monocrystalline model where deformation twinning involves the whole crystal for the nanocrystalline model, deformation twinning is rather localized in a fraction of the grains.

The profiles of the plastic deformation are shown in Fig. 9 for $U_p = 2.5$ km/s. Figures 9(a) to 9(c) show clearly an absence of wave splitting and a sharp plastic wave front. The well-defined particle velocity profile shown in Fig. 9(a) indicates that while the nanostructure is heterogeneous with grains of different sizes, shapes, and crystal orientations, the state of the plastic wave is well-defined and stable. The same well-defined state is shown by the density profile shown in Fig. 9(b) indicating a sharp compression of the nc-SiC model

from 3.1 g/cm³ to 4.1 g/cm³ at the wave front. The stress profile shown in Fig. 9(c) indicates that the shear stress that is built quickly at the shock front is gradually released as the plastic wave develops until a nearly hydrostatic state is reached. The *xy* displacement for the nanocrystalline sample, shown in Fig. 9(d), shows a highly inhomogeneous distribution of values between ∼2 and 8 Å, which is a result of the combination of grain boundary sliding and deformation twinning mechanisms.

Possibly the most important result from shock investigations is the shear stress generated at the Hugoniot elastic limit, which provides a good estimate of the strength of the material. In Fig. 10, the shear stresses for low particle velocities are plotted until the Hugoniot elastic limit, where the values are maximum. Data for shear stress outside this range, i.e., at very low impact velocities or at velocities beyond the Hugoniot elastic limit, are prone to large fluctuations and are not plotted here. The monocrystalline strengths predicted are 15.2, 30.9, and 31.4 GPa for ⟨001⟩, ⟨110⟩, and ⟨111⟩ directions and 12.3 GPa for the nc-SiC model. Considering that the strength of defect free monocrystalline SiC is expected to be higher than for polycrystalline samples, the results are consistent with the values measured experimentally[16] in the range 8–16 GPa. In particular, the strength calculated for the nanocrystalline sample agrees very well with experiments in face of the expected loss of strength due to the softer interface material, which constitutes a large fraction of the nanocrystalline sample.
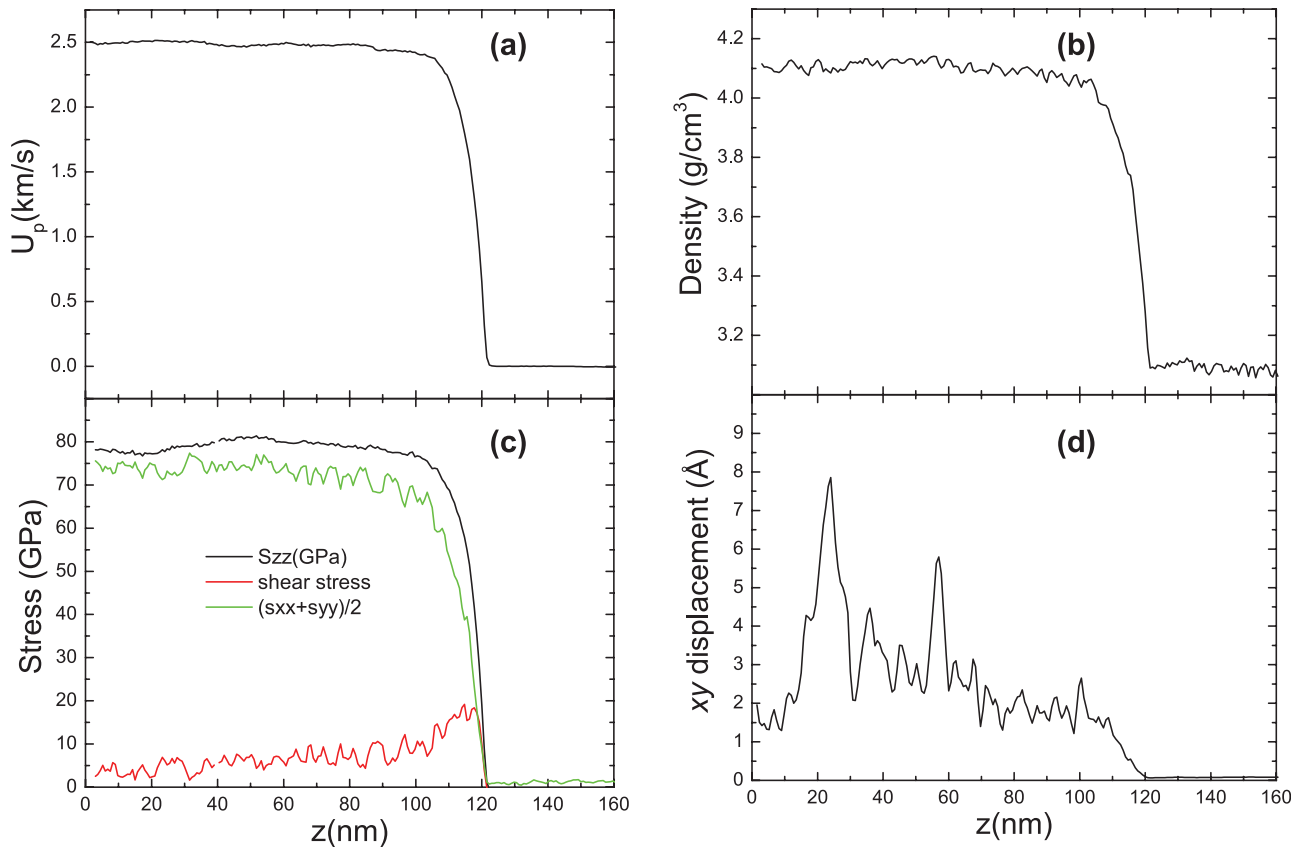
FIG. 9. Shock profiles of plastic deformation in the nc-SiC model for $U_p = 2.5$ km/s. (a) and (b) Particle velocity and density profiles indicating a sharp shock front with no split waves. (c) Stress profile indicating the release of shear stress generated at the shock front by the plastic deformations. (d) *xy* displacement profile indicating buildup of large atomic displacement of up to 8 Å in the plastic wave twinned regions.

IV. CONCLUSIONS

Plane shock loading on mono- and nanocrystalline SiC ceramics was performed using molecular dynamics simulations with the aim of revealing the interplay between elastic compression, plastic deformation, and the structural phase transformation. We observed distinct shock wave regimes: elastic, intermediate, plastic, structural phase transformation, and over-driven, by increasing the particle velocity irrespective of the crystallographic directions and temperatures employed in the
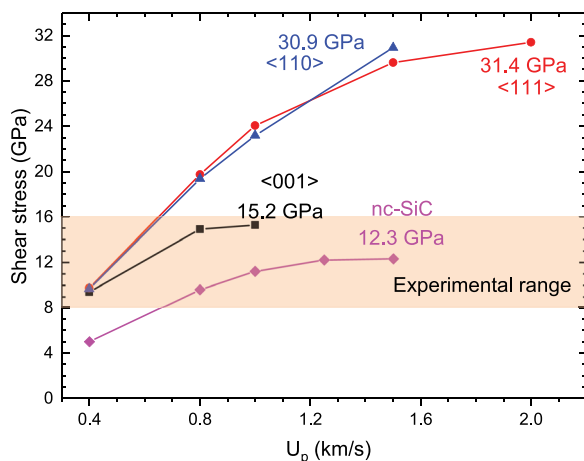

FIG. 10. Shear strength in the elastic regimes for crystalline and nanocrystalline samples. The shear stress at the Hugoniot state indicates the strength of SiC.

systems. The particle velocity range chosen is 0.1–6.0 km/s, and it accesses all shock wave regimes. When U_p is less than 0.8–1.9 km/s, only elastic uniaxial compression is observed. At about 1 km/s, the elastic compression generates an intermediate phase. At about 1.5 km/s, a plastic wave is generated which is indicated by a large *xy* displacement in the shock profile and clear deformation twinning in the atomic structure models. When the generated pressure is higher than 90 GPa, a zinc blende to rock salt structural phase transformation is triggered. Finally, the structural phase transformation overtakes the elastic wave at ∼5.0–6.0 km/s, and a single overdriven wave is observed. The induced shear stress is promptly relaxed by the plastic and SPT waves. In contrast, while all shock regimes are present in the nanocrystalline sample, it has an absence of wave splits and shows a seamless increase in shock velocity with particle velocity. The predicted shock Hugoniot are in excellent agreement with experimental data. In particular, the calculated strengths at the Hugoniot elastic limit 15.2, 31.4, and 30.9 GPa for ⟨001⟩, ⟨110⟩, and ⟨111⟩ directions and 12.3 GPa for the nanocrystalline sample are in excellent agreement with the experimental range of values for polycrystalline samples. These results provide important atomistic insights into the shock wave behavior of mono-and nanocrystalline ceramics.

[1]H. Ko, A. Kaczmarowski, I. Szlufarska, and D. Morgan, "Optimization of self-interstitial clusters in 3C-SiC with genetic algorithm," J. Nucl. Mater. **492**, 62–73 (2017).

[2]Y. Katoh, L. L. Snead, I. Szlufarska, and W. J. Weber, "Radiation effects in SiC for nuclear structural applications," Curr. Opin. Solid State Mater. Sci. **16**, 143–152 (2012).

[3]J. Deng, H. Ko, P. Demkowicz, D. Morgan, and I. Szlufarska, "Grain boundary diffusion of Ag through polycrystalline SiC in TRISO fuel particles," J. Nucl. Mater. **467**, 332–340 (2015).

[4]W. Aiguo and H. J. Rack, "Abrasive wear of silicon carbide particulate— and whisker-reinforced 7091 aluminum matrix composites," Wear **146**, 337–348 (1991).

[5]J.-C. Zhao and J. H. Westbrook, "Ultrahigh-temperature materials for jet engines," MRS Bull. **28**, 622–630 (2003).

[6]T. J. Holmquist and G. R. Johnson, "Response of silicon carbide to high velocity impact," J. Appl. Phys. **91**, 5858–5866 (2002).

[7]M. Flinders, D. Ray, A. Anderson, and R. A. Cutler, "High-toughness silicon carbide as armor," J. Am. Ceram. Soc. **88**, 2217–2226 (2005).

[8]M. E. Kipp and D. E. Grady, "Shock phase transformation and release properties of aluminum nitride," J. Phys. III Colloq. **4**, C8-249 (1994).

[9]D. E. Grady, "Shock-wave compression of brittle solids," Mech. Mater. **29**, 181–203 (1998).

[10]G. R. Johnson, T. J. Holmquist, and S. R. Beissel, "Response of aluminum nitride (including a phase change) to large strains, high strain rates, and high pressures," J. Appl. Phys. **94**, 1639–1646 (2003).

[11]D. E. Grady, "Shock-wave strength properties of boron carbide and silicon carbide," J. Phys. IV **4**, 385–391 (1994).

[12]N. Bourne, J. Millett, and I. Pickup, "Delayed failure in shocked silicon carbide," J. Appl. Phys. **81**, 6019 (1997).

[13]J. C. F. Millett, N. K. Bourne, and D. P. Dandekar, "Delayed failure in a shock-loaded silicon carbide," J. Appl. Phys. **97**, 113513 (2005).

[14]R. F. Trunin, L. F. Gudarenko, M. V. Zhernokletov, and G. V. Simakov, *Experimental Data on Shock Compression and Adiabatic Expansion of Condensed Matter* (Russian Federal Nuclear Center - VNIIEF, Sarov, 2001).

[15]T. Sekine and T. Kobayashi, "Shock compression of 6H polytype SiC to 160 GPa," Phys. Rev. B **55**, 8034–8037 (1997).

[16]T. J. Vogler, W. D. Reinhart, L. C. Chhabildas, and D. P. Dandekar, "Hugoniot and strength behavior of silicon carbide," J. Appl. Phys. **99**, 23512 (2006).

[17]I. A. Balagansky, A. I. Balagansky, S. V. Razorenov, and A. V. Utkin, "Evolution of shock waves in silicon carbide rods," AIP Conf. Proc. **845**, 835–838 (2006).

[18]A. S. Savinykh, G. I. Kanel, S. V. Razorenov, and V. I. Rumyantsev, "Evolution of shock waves in SiC ceramic," Tech. Phys. **58**, 973–977 (2013).

[19]M. O. Steinhauser, K. Grass, E. Strassburger, and A. Blumen, "Impact failure of granular materials - Non-equilibrium multiscale simulations and high-speed experiments," Int. J. Plast. **25**, 161–182 (2009).

[20]B. L. Holian and G. K. Straub, "Molecular dynamics of shock waves in three-dimensional solids: Transition from nonsteady to steady waves in perfect crystals and implications for the Rankine-Hugoniot conditions," Phys. Rev. Lett. **43**, 1598–1600 (1979).

[21]D. Robertson, D. Brenner, and C. White, "Split shock waves from molecular dynamics," Phys. Rev. Lett. **67**, 3132–3135 (1991).

[22]D. Brenner, D. Robertson, M. Elert, and C. White, "Detonations at nanometer resolution using molecular dynamics," Phys. Rev. Lett. **76**, 2202–2202 (1996).

[23]K. Nomura *et al.*, "Dynamic transition in the structure of an energetic crystal during chemical reactions at shock front prior to detonation," Phys. Rev. Lett. **99**, 148303 (2007).

[24]M. Vedadi *et al.*, "Structure and dynamics of shock-induced nanobubble collapse in water," Phys. Rev. Lett. **105**, 14503 (2010).

[25]B. L. Holian, "Plasticity induced by shock waves in nonequilibrium molecular-dynamics simulations," Science **280**, 2085–2088 (1998).

[26]T. Germann, B. Holian, P. Lomdahl, and R. Ravelo, "Orientation dependence in molecular dynamics simulations of shocked single crystals," Phys. Rev. Lett. **84**, 5351–5354 (2000).

[27]K. Kadau, T. C. Germann, P. S. Lomdahl, and B. L. Holian, "Microscopic view of structural phase transitions induced by shock waves," Science **296**, 1681–1684 (2002).

[28]E. M. Bringa *et al.*, "Ultrahigh strength in nanocrystalline materials under shock loading," Science **309**, 1838–1841 (2005).

[29]P. S. Branicio *et al.*, "Atomistic damage mechanisms during hypervelocity projectile impact on AlN: A large-scale parallel molecular dynamics simulation study," J. Mech. Phys. Solids **56**, 1955–1988 (2008).

[30]P. S. Branicio, R. K. Kalia, A. Nakano, and P. Vashishta, "Nanoductility induced brittle fracture in shocked high performance ceramics," Appl. Phys. Lett. **97**, 111903 (2010).

[31]P. S. Branicio, "Atomistic mechanisms in silicon carbide nanostructures," J. Comput. Theor. Nanosci. **9**, 1870–1880 (2012).

[32]X. D. Han *et al.*, "Low-temperature in situ large strain plasticity of ceramic SiC nanowires and its atomic-scale mechanism," Nano Lett. **7**, 452–457 (2007).

[33]W. H. Li, X. H. Yao, P. S. Branicio, X. Q. Zhang, and N. B. Zhang, "Shock-induced spall in single and nanocrystalline SiC," Acta Mater. **140**, 274 (2017).

[34]W. H. Lee, X. H. Yao, W. R. Jian, and Q. Han, "High-velocity shock compression of SiC via molecular dynamics simulation," Comput. Mater. Sci. **98**, 297–303 (2015).

[35]P. Vashishta, R. K. Kalia, A. Nakano, and J. P. Rino, "Interaction potential for silicon carbide: A molecular dynamics study of elastic constants and vibrational density of states for crystalline and amorphous silicon carbide," J. Appl. Phys. **101**, 103515 (2007).

[36]F. Shimojo *et al.*, "Molecular dynamics simulation of structural transformation in silicon carbide under pressure," Phys. Rev. Lett. **84**, 3338–3341 (2000).

[37]H. Kikuchi *et al.*, "Brittle dynamic fracture of crystalline cubic silicon carbide (3C-SiC) via molecular dynamics simulation," J. Appl. Phys. **98**, 103524 (2005).

[38]H. Tsuzuki, J. P. Rino, and P. S. Branicio, "Dynamic behaviour of silicon carbide nanowires under high and extreme strain rates: A molecular dynamics study," J. Phys. D: Appl. Phys. **44**, 55405 (2011).

[39]P. S. Branicio, A. Nakano, R. K. Kalia, and P. Vashishta, "Shock loading on AlN ceramics: A large scale molecular dynamics study," Int. J. Plast. **51**, 122–131 (2013).

[40]P. S. Branicio, R. K. Kalia, A. Nakano, and P. Vashishta, "Shock-induced structural phase transition, plasticity, and brittle cracks in aluminum nitride ceramic," Phys. Rev. Lett. **96**, 65502 (2006).

[41]C. Zhang, R. K. Kalia, A. Nakano, P. Vashishta, and P. S. Branicio, "Deformation mechanisms and damage in α-alumina under hypervelocity impact loading," J. Appl. Phys. **103**, 83508 (2008).

[42]W. H. Li, X. Yao, and X. Q. Zhang, "Planar impacts on nanocrystalline SiC: A comparison of different potentials," J. Mater. Sci. **53**, 6636 (2018).

[43]W. Brostow, J.-P. Dussault, and B. L. Fox, "Construction of Voronoi polyhedra," J. Comput. Phys. **29**, 81–92 (1978).

[44]J. Y. Zhang *et al.*, "Superplastic nanocrystalline ceramics at room temperature and high strain rates," Scr. Mater. **69**, 525–528 (2013).

[45]P. S. Branicio and D. J. Srolovitz, "Local stress calculation in simulations of multicomponent systems," J. Comput. Phys. **228**, 8467–8479 (2009).

[46]J. Zhang and P. S. Branicio, "Molecular dynamics simulations of plane shock loading in SiC," Procedia Eng. **75**, 150–153 (2014).

[47]P. S. Branicio and J. Zhang, "Atomistic modeling of shock loading in SiC ceramics," MRS Proc. **1535**, 370 (2013).

[48]J. P. Rino *et al.*, "Short- and intermediate-range structural correlations in amorphous silicon carbide: A molecular dynamics study," Phys. Rev. B **70**, 45207 (2004).

[49]E. M. Bringa *et al.*, "Atomistic shock Hugoniot simulation of single-crystal copper," J. Appl. Phys. **96**, 3793–3799 (2004).

[50]K. Kadau *et al.*, "Shock waves in polycrystalline iron," Phys. Rev. Lett. **98**, 135701 (2007).

[51]M. Durandurdu, "Pressure-induced phase transition of SiC," J. Phys.: Condens. Matter **16**, 4411–4417 (2004).